

# Effects of Viscosity on Sloshing Cold Fronts in Galaxy Clusters

Ming-Hsueh Hsieh,<sup>1</sup>★ H.-Y. Karen Yang,<sup>1,2,3</sup>† and John ZuHone<sup>4</sup>

<sup>1</sup>Institute of Astronomy, National Tsing Hua University, Hsinchu 30013, Taiwan (R.O.C.)

<sup>2</sup>Center for Informatics and Computation in Astronomy, National Tsing Hua University, Hsinchu 30013, Taiwan (R.O.C.)

<sup>3</sup>Physics Division, National Center for Theoretical Sciences, Taipei 106017, Taiwan (R.O.C.)

<sup>4</sup>Center for Astrophysics | Harvard & Smithsonian, 60 Garden Street, Cambridge, MA 02138, USA

Accepted XXX. Received YYY; in original form ZZZ

## ABSTRACT

The viscous properties of the intracluster medium (ICM) remain poorly constrained. Cold fronts—sharp discontinuities formed during cluster mergers—offer a potential avenue to probe the effective viscosity of the ICM. Velocity shear across these fronts should generate Kelvin–Helmholtz instabilities (KHI), unless viscosity or magnetic tension suppresses them. We perform cluster merger simulations incorporating four ICM viscosity models: (A) inviscid, (B) isotropic Spitzer viscosity, (C) anisotropic Braginskii viscosity, and (D) Braginskii viscosity limited by microinstabilities. The isotropic Spitzer viscosity (case B) strongly suppresses KHI, producing smooth cold front surfaces, while the inviscid (A) and microinstability-limited (D) cases show prominent ripples. The Braginskii case (C) yields intermediate suppression. We also vary the plasma  $\beta$  parameter ( $\beta \approx 100$  and 1600) to examine how a changing magnetic field strength affects the results. Stronger magnetic fields further suppress KHI, leading to smoother fronts and reduced differences between different viscosity models, while also widening the range of permitted pressure anisotropies when microinstability-based limiters are present. These results indicate that both viscosity and magnetic fields play crucial roles in stabilising sloshing cold fronts in galaxy clusters.

**Key words:** sloshing motions – viscosity – cluster merging – methods: numerical

## 1 INTRODUCTION

X-ray observations have revealed valuable information about the intracluster medium (ICM), the hot plasma filling the dark matter halos of galaxy clusters. Although it is known that the ICM is a weakly collisional, magnetized plasma, key microphysical properties such as the strength and configuration of the magnetic field, as well as the effective viscosity, remain poorly constrained. In particular, it is unclear whether the viscosity in the ICM is isotropic or anisotropic, and how it combines with magnetic fields to suppress hydrodynamic instabilities such as the Kelvin–Helmholtz instability (KHI). Numerical simulations provide a powerful tool for probing these unknowns and testing theoretical models of ICM microphysics.

X-ray observations of galaxy clusters often show sharp surface brightness discontinuities. Spectral analysis of the emission on either side of these images has revealed that in most cases the brighter side of the edge is the colder side (Markevitch et al. 2000; Vikhlinin et al. 2001). Brighter regions correspond to denser areas since the X-ray surface brightness depends on the square of the density. Hence, these jumps in gas density have been called “cold fronts” (for a detailed review, see Markevitch & Vikhlinin 2007). Observations indicate that cold fronts can form during major cluster mergers; a prominent example is the “Bullet Cluster” (Markevitch et al. 2002). However, cold fronts are also observed in relaxed clusters that do not exhibit

evidence of major mergers. In these cases, the cold fronts are thought to arise from sloshing motions from encounters with small infalling groups or subclusters that gravitationally perturb the cluster core (Ascasibar & Markevitch 2006; Tittley & Henriksen 2005; ZuHone et al. 2010). During a minor merger or gravitational perturbation, a subcluster passes near the core of a larger galaxy cluster. This encounter displaces the dense, low-entropy gas at the center of the cluster from the minimum of the gravitational potential. Unlike the collisionless dark matter, the intracluster gas is subject to ram pressure from the surrounding medium and is temporarily pushed outward. Once the external perturbation subsides, the gravitational potential of the cluster pulls the displaced gas back toward the center. Due to the conservation of angular momentum and the asymmetry of the initial displacement, the gas does not return in a straight line. Instead, it begins to oscillate—or “slosh”—in the gravitational potential well. These motions generate spiral-like patterns and create sharp contact discontinuities in density and temperature, observed as cold fronts in X-ray surface brightness maps.

The KHI is a type of fluid instability in a shear layer, which causes the interface of the layer to become unstable to small perturbations and form structures such as ripples. At the interfaces of cold fronts in clusters, the velocity difference between the inner part and the outer part of the interface produces a shear which is caused by the sloshing motions. This velocity shear causes the interface to become susceptible to the KHI. Early X-ray observations showed that the cold front interfaces typically appeared smooth (Markevitch et al. 2000; Vikhlinin et al. 2001) and free from the ripples which would serve as

★ E-mail: arthur20010514@gmail.com

† E-mail: hyang@phys.nthu.edu.tw

the evidence of KHI. However, with the benefit of deeper exposures providing better statistics, several cold fronts have been found to exhibit evidence of the KHI, such as ripple-like or eddy structures (Werner et al. 2016; Su et al. 2017; Wang & Markevitch 2018). More observational data are still required to fully determine the morphology of cold fronts. However, even in cases where eddy-like structures are observed, the growth of the KHI appears to be partially suppressed to some extent (with an estimated effective viscosity of  $\sim 10\%$  of the Spitzer value in Wang & Markevitch 2018 and  $\sim 5\%$  in Werner et al. 2016). Previous simulations (ZuHone et al. 2011; Roediger et al. 2013b; ZuHone et al. 2015) suggest that both viscosity and magnetic fields can play a significant role in suppressing the KHI in sloshing cold fronts. These works explore different physical scenarios: ZuHone et al. (2011) focuses on the influence of varying initial plasma  $\beta$  values, while ZuHone et al. (2015) examines the effects of different viscosity models on the development of cold front structures. However, it is not clear which mechanisms are more dominant in suppressing the KHI.

In the ICM, Coulomb collisions between ions and electrons are relatively infrequent due to the low density and high temperature, resulting in a large mean free path. Under such weakly collisional conditions, the classical Spitzer formulation (Spitzer 1962) becomes invalid. In addition, the presence of magnetic fields introduces anisotropy in transport processes, since the Larmor radii of the electrons and ions are many orders of magnitude smaller than the Coulomb mean free paths. In such a magnetized plasma, momentum and heat are transported more efficiently along magnetic field lines than across them, leading to Braginskii viscosity, an anisotropic form of viscous stress originating from pressure anisotropies in the weakly collisional, magnetized medium (Braginskii 1965; Schekochihin et al. 2005). Furthermore, recent plasma physics simulations have shown that Larmor-scale kinetic instabilities, such as the firehose and mirror instabilities, would be triggered and act to regulate pressure anisotropy and suppress viscosity in the ICM (Kunz et al. 2014). How these microphysics instabilities impact the cold front structures still remain unsolved. Inspired by them, we attempt to understand the roles of microphysics in cluster mergers through numerical simulations.

Our simulations aim to explore the nature of the ICM viscosity in the context of the cores of relaxed galaxy clusters, where sloshing cold fronts are found. By incorporating different viscosity models and magnetic field strengths, we compare the simulated cold fronts with observations, seeking to provide insights and predictions for future research.

This paper is organized as follows.

- Section 2 describes the numerical setup and simulation methods, including the initial conditions, viscosity models, and the governing equations.
- Section 3 presents the simulation results, focusing on how different viscosity models and magnetic field strengths affect the stability and morphology of sloshing cold fronts.
- Section 4 discusses the results and compares them with previous studies.
- Section 5 presents a summary of this work.

## 2 METHODS

We conduct 3D Braginskii-magnetohydrodynamic (MHD) simulations of binary cluster mergers using FLASH, an adaptive-mesh refinement (AMR) MHD code. The algorithms employed in FLASH are detailed in Fryxell et al. (2000) and Dubey et al. (2009). Our

cluster merger simulations incorporated four different viscosity models: (A) no viscosity, (B) isotropic Spitzer viscosity, (C) Braginskii viscosity, and (D) Braginskii viscosity limited by microscopic plasma instabilities. These assumptions follow the approaches outlined in Kingsland et al. (2019) and the equations are provided in Section 2.1. The cluster merger scenario follows that of ZuHone et al. (2011) and will be described in detail in Section 2.2. For each of the four assumptions, we also introduce varying magnetic energy to investigate how magnetic field strength influences the impact of viscosity on the cold fronts and sloshing motions.

### 2.1 Equations

In our cluster merger simulations, we solve the Braginskii-MHD equations as follows:

$$\frac{\partial \rho}{\partial t} + \nabla \cdot (\rho \mathbf{v}) = 0 \quad (1)$$

$$\frac{\partial(\rho \mathbf{v})}{\partial t} + \nabla \cdot (\rho \mathbf{v} \mathbf{v} - \frac{\mathbf{B}\mathbf{B}}{4\pi} + p_{\text{tot}}\mathbf{I}) = \rho \mathbf{g} - \nabla \cdot \Pi \quad (2)$$

$$\frac{\partial E}{\partial t} + \nabla \cdot [\mathbf{v}(E + p_{\text{tot}}) - \frac{\mathbf{B}(\mathbf{v} \cdot \mathbf{B})}{4\pi}] = \rho \mathbf{g} \cdot \mathbf{v} - \nabla \cdot (\Pi \cdot \mathbf{v}) \quad (3)$$

$$\frac{\partial \mathbf{B}}{\partial t} + \nabla \cdot (\mathbf{v}\mathbf{B} - \mathbf{B}\mathbf{v}) = 0, \quad (4)$$

where  $\rho$  is gas density,  $\mathbf{v}$  is gas velocity,  $E$  is the total energy density,  $\mathbf{B}$  is the magnetic field,  $\mathbf{I}$  is the identity tensor, and  $p_{\text{tot}} = p + p_B = p + B^2/(8\pi)$  is the total (thermal plus magnetic) pressure. In this work, we consider several models for the viscosity tensor  $\Pi$ . For the case of isotropic viscosity, we adopt the Spitzer viscosity (Spitzer 1962), appropriate for a collisional, non-magnetized, fully ionized plasma. The isotropic viscosity tensor is defined as

$$\Pi_{\text{iso}} = -\mu \left[ \nabla \mathbf{v} + (\nabla \mathbf{v})^\top - \frac{2}{3} \nabla \cdot \mathbf{v} \right], \quad (5)$$

where  $\mu$  is the dynamic viscosity coefficient

$$\mu = 2.2 \times 10^{-15} \frac{T^{5/2}}{\ln \Lambda} \text{ g cm}^{-1} \text{ s}^{-1}, \quad (6)$$

where  $\ln \Lambda = 40$  is the Coulomb logarithm following the approximation of ICM conditions (e.g., Roediger et al. 2013b).

For the anisotropic Braginskii viscosity, it can be expressed as (Braginskii 1965):

$$\Pi_{\text{aniso}} = -3\mu(\mathbf{b}\mathbf{b} - \frac{1}{3}\mathbf{I})(\mathbf{b}\mathbf{b} - \frac{1}{3}\mathbf{I}) : \nabla \mathbf{v}, \quad (7)$$

where  $\mathbf{b}$  is the unit vector of the magnetic field. For non-magnetized, collisional fluids, the isotropic Spitzer viscosity is a good approximation. However, in the magnetized, weakly collisional ICM, the gyro-radii of charged particles are very small compared to the collisional mean free path of the particles, which leads to anisotropic or Braginskii viscosity. In essence, the Braginskii viscosity arises from pressure anisotropy due to the conservation of the adiabatic invariants of charged particles within the magnetized plasma, which is balanced by its relaxation via ion-ion collisions (Schekochihin et al. 2005). This relationship is described by

$$p_{\perp} - p_{\parallel} = 0.96 \frac{p_i}{v_{ii}} \frac{d}{dt} \ln \frac{B^3}{\rho^2} = 3\mu(\mathbf{b}\mathbf{b} - \frac{1}{3}\mathbf{I}) : \nabla \mathbf{v}, \quad (8)$$

where  $v_{ii}$  is the ion-ion collision frequency and  $p_i$  is thermal pressure

for ions. We apply both isotropic and anisotropic models of viscosity in our simulations to determine which fares better in comparison to the observations.

Plasma physics simulations have found that Larmor-scale instabilities (firehose instability and mirror instability) would be triggered and act to regulate the pressure anisotropy (Kunz et al. 2014). They found that the pressure anisotropy should be limited within the microinstability thresholds:

$$-\frac{2}{\beta} \leq \Delta_p \equiv \frac{p_{\perp} - p_{\parallel}}{p} \leq \frac{1}{\beta}, \quad (9)$$

where  $\beta = p/p_B$  is the plasma  $\beta$  parameter, indicating the ratio of thermal to magnetic pressures. The left-hand side of equation 9 corresponds to the firehose instability ( $\Delta_p < -\frac{2}{\beta}$ ; Rosenbluth 1956; Chandrasekhar et al. 1958; Parker 1958), and the right-hand side corresponds to the mirror instability (Barnes 1966; Hasegawa 1969; Southwood & Kivelson 1993; Hellinger 2007,  $\Delta_p > \frac{1}{\beta}$ ). The firehose instability occurs when the pressure along the magnetic field lines is greater than the pressure perpendicular to the field to such an extent that it overcomes the restoring force of the magnetic tension, leading to the unstable growth of Alfvénic perturbations. In contrast, the mirror instability occurs when the pressure perpendicular to the magnetic field lines is greater than the pressure parallel to the field by an extent that exceeds the magnetic pressure. In this case, the plasma will expand sideways, distorting the magnetic field into local magnetic “bottles”. These bottle structures trap particles which bounce between mirror structures on either side. At the ends of the bottles, particles can escape due to adiabatic invariance, lowering the thermal pressure and causing the magnetic field lines to further contract, reinforcing the instability. In either case, the fastest-growing modes of the instability are near the Larmor scale (Kunz et al. 2014; Melville et al. 2016). These modes efficiently pitch-angle scatter particles, reducing the anisotropy and restoring marginal stability. This effect acts as a feedback mechanism to regulate the anisotropy. In the weakly collisional, magnetized ICM, the high plasma- $\beta$  conditions are likely to trigger both firehose and mirror instabilities. Therefore, in one of our models, we impose constraints on pressure anisotropy to account for the regulation imposed by these microphysical instabilities.<sup>1</sup>

## 2.2 Initial conditions

We simulate the merger of two galaxy clusters, following the setup by ZuHone et al. (2011). The primary cluster is modeled as a cool-core cluster with  $M \sim 1.25 \times 10^{15} M_{\odot}$ , while the mass of the sub-cluster is  $2.5 \times 10^{14} M_{\odot}$ . For the dark matter profile of the cluster, the Hernquist (1990) profile is utilized:

$$\rho_{\text{DM}}(r) = \frac{M_{\text{tot}}}{2\pi a^3} \frac{1}{(r/a)(1+r/a)^3}. \quad (10)$$

Here,  $M_{\text{tot}}$  is the total mass, and  $a = 600$  kpc is the scale length of the dark matter halo.

The sub-cluster is initially positioned at a distance  $d = 3$  Mpc from the main cluster at the beginning of the simulations. The initial impact parameter is  $b = 0.5$  Mpc, and the relative velocity of sub-cluster is  $1466 \text{ km s}^{-1}$  at the beginning of the simulation, resulting in the total

<sup>1</sup> We note that there are other relevant bounds for the pressure anisotropy in plasmas such as the ICM due to the oblique firehose instability (Hellinger & Matsumoto 2000; Hellinger & Trávníček 2008; Bott et al. 2021) or ion-cyclotron instability (Gary et al. 1997; Ley et al. 2024). For simplicity, we do not include these bounds in the current study, but will include them in future work.

kinetic energy being half of its potential energy. The two clusters come closest around  $t = 1.5$  Gyr, and after this epoch, the sloshing motions begin. In Section 3, we present data at 2.2 Gyr and 4 Gyr to compare the physical parameters after the core passage of the merger.

The simulation box is a cube with a side length of 8 Mpc, refined using AMR in order to reduce computational expense. Our primary focus lies in the cluster center, where sloshing motions predominantly occur. The refinement criteria in our simulations are based on gradients of gas density and temperature, and refinement within a fixed radius of 150 kpc from the main cluster center. The coarsest cell size on our AMR grid is  $\Delta x = 62.5$  kpc and the finest cell size is  $\Delta x = 3.9$  kpc. The scales of the sloshing motions are approximately 50-200 kpc. Thus, this resolution is sufficient for analyzing the sloshing motions in different viscosity environments.

In our simulations, we utilize the kinematic viscosity ( $\nu = \mu/\rho$ ) to compute the simulation time step. With an explicit solver for viscosity, the simulation time step must obey the inequality  $\Delta t \leq \frac{1}{2} \frac{\Delta x^2}{\nu}$ , where  $\Delta x$  is the grid size. Higher kinematic viscosity leads to smaller time steps and significantly increases the computational time. To address this issue, we impose an upper limit on the kinematic viscosity, such that  $\nu \leq 10^{31} \text{ cm}^2 \text{ s}^{-1}$ . This ceiling is somewhat arbitrary but necessary for maintaining computational efficiency. In our simulations,  $\nu$  typically ranges from  $\sim 10^{28}$  to  $10^{31} \text{ cm}^2 \text{ s}^{-1}$  in the central region where our analyses are conducted. Given this range, we expect that the imposed ceiling does not significantly affect the overall results.

The simulation suite comprises four models of ICM viscosity. The first model does not involve any viscosity. The second model includes isotropic Spitzer viscosity, known for effectively suppressing KHI (Roediger et al. 2013a; Roediger et al. 2013b), though it might considered too extreme for some of the observed cold fronts (Werner et al. 2016). The third model incorporates Braginskii viscosity, expected to operate in magnetized plasmas, in which momentum diffusion occurs predominantly along the magnetic field lines. The fourth model combines Braginskii viscosity with microinstabilities, introducing effects that limit pressure anisotropies. In Section 3, we present and compare the results of the four models: (A) no viscosity, (B) isotropic viscosity, (C) anisotropic viscosity, and (D) anisotropic viscosity limited by the microinstabilities.

For the initial magnetic field, we follow ZuHone et al. (2011) and ZuHone et al. (2012) to set up a tangled magnetic field with a power-law spectrum ranging from 500 kpc to 43 kpc. In each of the four viscosity models, we introduce two levels of magnetic energy in the ICM to investigate the influence of magnetic field strength on cluster mergers. To facilitate interpretation, we employ the plasma  $\beta$  parameter to quantify the amount of magnetic energy in the simulations. In the ICM, the plasma  $\beta$  typically has a value between  $\sim 100$ -1000 due to the weak magnetic field. In this paper, we use two values of plasma  $\beta$  ( $\beta = 100$  and  $\beta = 1600$ ) to examine the potential impact of the initial magnetic field strength on the sloshing cold fronts. The magnetic field plays an important role, because magnetic tension can suppress the KHI on its own (ZuHone et al. 2011). As already noted above, the magnetic field makes the viscosity anisotropic, and a stronger field strength widens the microinstability bounds. The setup of our simulations is summarized in Table 1.

## 3 RESULTS

In this section, we present our simulation results. All simulations discussed in Section 3.1 and 3.2 are initialized with  $\beta \sim 1600$ . Section 3.1 illustrates the evolution of the main cluster during the cluster merger. We delve into the effects of viscosity in detail in Section

**Table 1.** Eight simulations for different initial plasma  $\beta$  ( $\beta$ ) and different assumptions for ICM viscosity.

Simulation	Initial $\beta$	Assumption for ICM viscosity
A100	100	no viscosity
A1600	1600	no viscosity
B100	100	isotropic viscosity
B1600	1600	isotropic viscosity
C100	100	anisotropic viscosity
C1600	1600	anisotropic viscosity
D100	100	anisotropic viscosity limited by microinstabilities
D1600	1600	anisotropic viscosity limited by microinstabilities

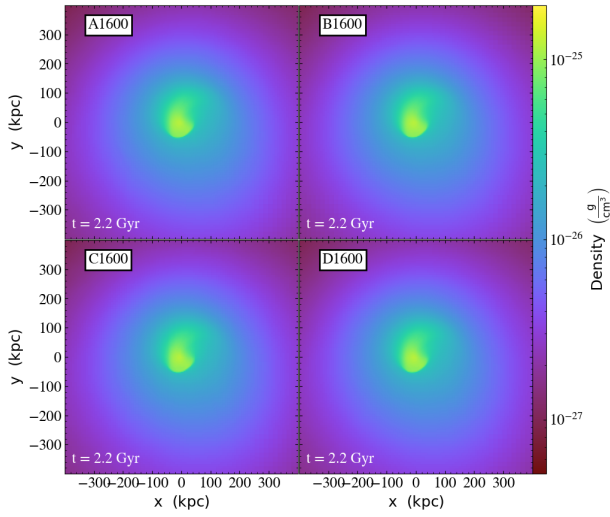


**Figure 1.** Density slice plots for high plasma  $\beta$  ( $\beta \sim 1600$ ) simulations at  $t = 2.2$  Gyr. The simulations are still in the early phase of the cluster merger. At this epoch, the cold fronts are already beginning to form, though there are no significant differences among the four models.

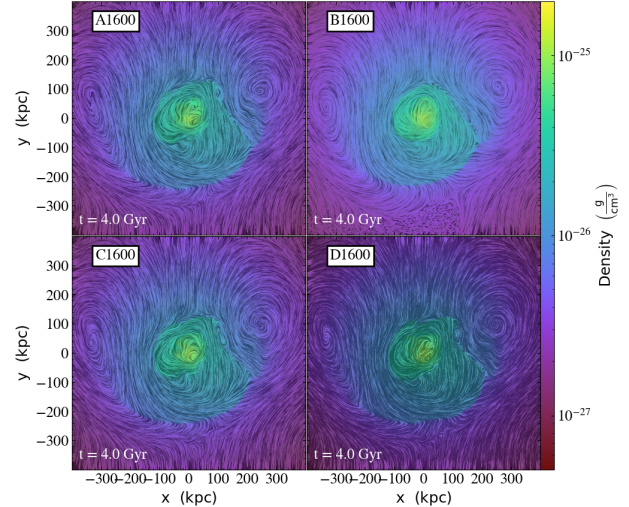
**3.2.** Finally, Section 3.3 presents simulations with  $\beta \sim 100$ . Our primary focus in this work is to investigate how the sloshing cold front influences the central part of the main cluster, and we present zoom-in figures to illustrate this effect.

### 3.1 Overall evolution

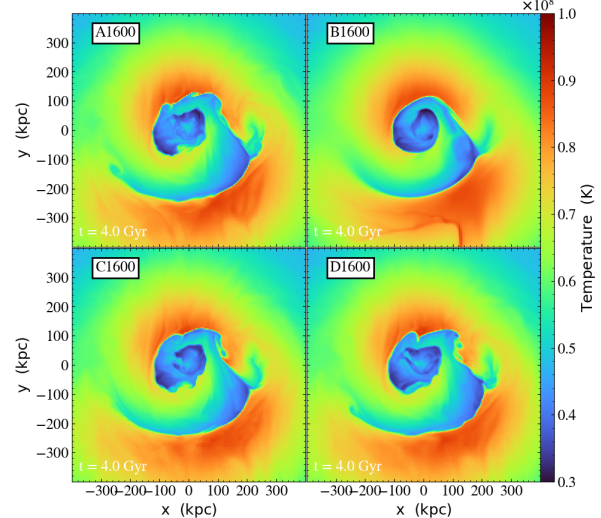
The entire simulation duration for the cluster merger spans  $\sim 5$  Gyr. Although the two clusters come closest around  $t = 1.5$  Gyr, it takes time for the cold front structures to form in the central part of the main cluster. We have chosen the epochs of 2.2 Gyr and 4.0 Gyr to represent the early and later phases of cold front formation, respectively.

Figure 1 shows slices of gas density at  $t = 2.2$  Gyr for cases A1600–D1600 when the cold fronts are just beginning to develop. Since the cold front structures are not yet well developed in the central region at  $t = 2.2$  Gyr, there are only minimal differences among the four cases. The structural similarity at this stage arises because there has not been sufficient time for the KHI to grow. In contrast, significant differences become apparent later ( $t = 4.0$  Gyr).

Figure 2 shows the density slices at  $t = 4.0$  Gyr. At this time, the cold front structures have become larger and more apparent. The KHI develop due to the velocity shear at the interface of sloshing cold



**Figure 2.** Density slice plots for high plasma  $\beta$  ( $\beta \sim 1600$ ) simulations at  $t = 4.0$  Gyr. Spiral-shaped cold fronts are apparent at this stage. The apparently stability of the cold front surfaces follows this order:  $B1600 > C1600 > D1600 \gtrsim A1600$ . The black lines represent line integral convolution of the velocity field in the  $x$ - $y$  plane, used to visualise the gas velocity structure.



**Figure 3.** Temperature slice plots for high plasma  $\beta$  ( $\beta \sim 1600$ ) simulations at  $t = 4.0$  Gyr. Due to the sloshing motions induced by the merger, the cool-core region becomes disturbed, with hot outer gas intruding inward and forming temperature discontinuities. These structures, known as cold fronts, are characterized by the inner regions being cooler than the outer regions.

fronts, which can be easily seen from the velocity streamlines overlaid. When the KHI develop, the cold fronts become unstable and small structures form along their interfaces such as the ripples in Figure 2. The degree of the KHI varies between different viscosity models. In the later part of our results, the main focus will be on  $t = 4.0$  Gyr. Figure 3 presents slices of the temperature for cases A1600–D1600. From the temperature slices one can more easily identify the cold fronts, as the gas temperature transitions from low to high values

across the interfaces, as illustrated in Figure 3. Temperature plays an important role in our simulations because the Spitzer viscosity is a strong function of temperature, following Equation 6.

Case A1600 exhibits more ripples along the cold fronts compared to other cases due to the presence of KHI, which arises from the absence of viscosity. In contrast, the cold fronts in Case B1600 show very smooth surfaces. The presence of isotropic viscosity at the full Spitzer strength prevents the KHI from developing entirely. In Cases C1600 and D1600 involving anisotropic viscosity, the ripples are more pronounced than in the isotropic case at the cold front interfaces. This is because momentum transport by viscosity is limited to the local magnetic field direction, resulting in a weaker effective suppression of the KHI. In Case D1600, due to the limits on the pressure anisotropy imposed by the plasma microinstabilities, the viscous flux and therefore the suppression of KHI is further reduced, making Cases A1600 and D1600 very similar. These differences are most pronounced for the inner cold fronts within  $r \sim 100$  kpc of the cluster center. As for the outermost cold front at a radius of  $\sim 200$  kpc, it has a very similar appearance in Cases A1600, C1600, and D1600, which can be attributed to the lower shear velocity across the surface that results in a longer timescale for the KHI to develop, and a higher viscosity due to the larger temperature (see Section 3.2).

Figure 4 presents slices of magnetic field strength for Cases A1600–D1600. During sloshing, the magnetic field lines are dragged along by the gas, causing the magnetic field to align with the surface of the cold fronts (Lyutikov 2006; Dursi 2007; Keshet et al. 2010; ZuHone et al. 2011). The velocity shear across the cold front stretches the magnetic field lines, thereby amplifying the magnetic field. As a result, the magnetic field becomes stronger and more ordered along the surface of the cold fronts. In Figure 4, the magnetic structures show the morphology of the layers at the interface of the cold fronts. The direction of these magnetic layers aligns with the surface of the cold fronts due to the sloshing motions. Figure 5 presents slice plots of the angle  $\theta$  between the magnetic field and velocity vectors for the  $\beta \sim 1600$  cases, expressed in terms of  $\cos \theta$ . The yellow regions correspond to areas where  $|\cos \theta| \approx 1$ , indicating a strong alignment between the directions of the magnetic field and the velocity. The alignment just inside the cold front interfaces is more prominent than outside, where the higher velocities arise from sloshing motions. The morphological similarity between Figures 4 and 5 provides strong evidence for this alignment effect, supporting the interpretation that sloshing-induced velocity shear organizes the magnetic field into layers that follow the cold front surfaces.

### 3.2 Effects of viscosity in the $\beta = 1600$ cases

Figure 6 shows the slices of Reynolds number for Cases B1600–D1600 at  $t = 4.0$  Gyr. The Reynolds number is defined as  $Re = \rho v L / \mu$ , where  $v$  is fluid velocity,  $L$  is characteristic length, and  $\mu$  is the dynamic viscosity coefficient defined in Equation 6. We choose  $L = 30$  kpc as the characteristic length for the scale of the sloshing cold front. Case A1600 is excluded due to the absence of viscosity in this case. The Reynolds number provides a straightforward estimate of the strength of viscosity and where its effects become significant. For large Reynolds numbers, the inertial forces significantly exceed viscous forces, leading to turbulence and the KHI. Conversely, for smaller Reynolds numbers, viscous forces are more important, with opposite effects. The Reynolds number is typically defined assuming isotropic viscosity. In the anisotropic cases (Cases C1600 and D1600), the situation becomes more complex, making it difficult to directly compare the efficacy of viscosity among different models using the Reynolds number alone. Nevertheless, it remains a useful diagnostic

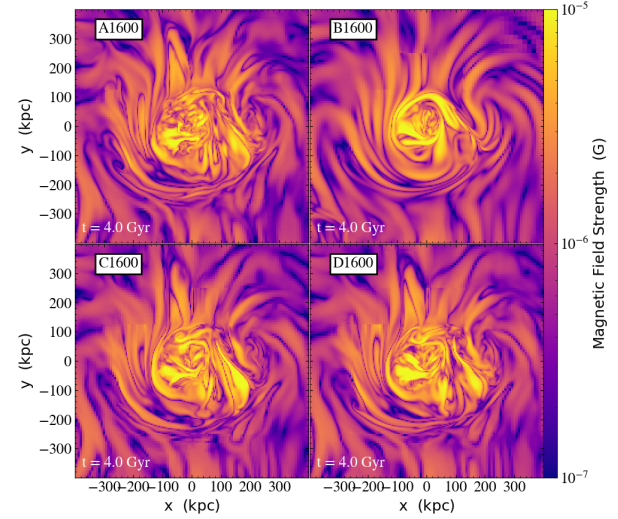


**Figure 4.** Magnetic field strength slice plots for high  $\beta$  ( $\beta \sim 1600$ ) simulations at  $t = 4.0$  Gyr. Velocity shear across the cold fronts stretches the magnetic field lines, leading to magnetic field amplification and the formation of magnetized layers aligned along the cold front surfaces.

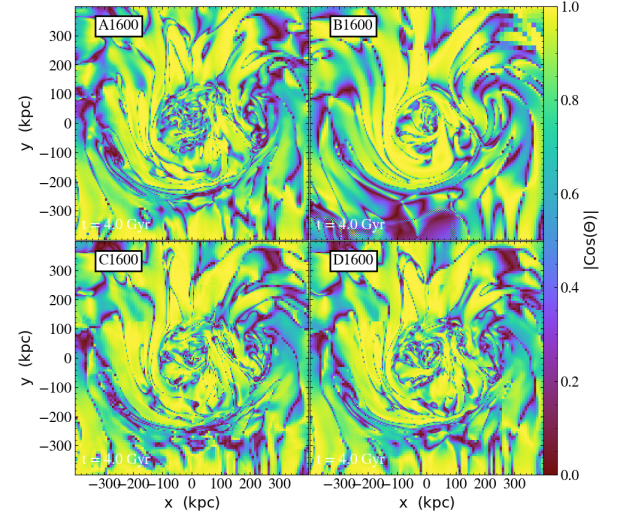


**Figure 5.** Angle between the magnetic field and velocity slice plots for high  $\beta$  ( $\beta \sim 1600$ ) simulations at  $t = 4.0$  Gyr. Because of the weaker magnetic tension in the high  $\beta$  environment, the magnetic fields are more easily stretched by sloshing motions, enhancing their alignment (yellow regions).

in terms of where viscosity could play a role. Roediger et al. (2013a) demonstrated using plane-parallel simulations of the development of KHI at cold front-like surfaces that the critical Reynolds number for the suppression of KHI is  $\sim 30$  (assuming a density contrast of  $\sim 2$  and isotropic viscosity with a Spitzer dependence).

One can see from Figure 6 that the Reynolds numbers in the inner regions of the cold fronts are higher than those in the outer regions, primarily due to the temperature and velocity structure of the ICM. As shown in Figure 3 and discussed in Section 3.1, the central part of the main cluster has lower temperatures, which leads to a smaller dynamic

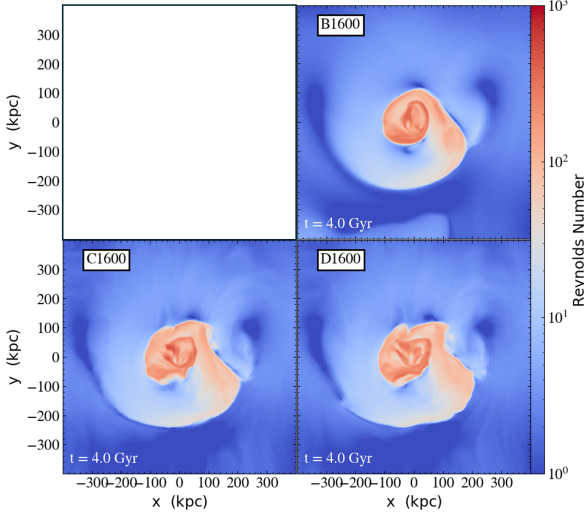


**Figure 6.** Reynolds number slice plots for high  $\beta$  ( $\beta \sim 1600$ ) simulations at  $t = 4.0$  Gyr. High Reynolds numbers in the central region indicate that the role of viscosity is less significant, favoring the development of the KHI and turbulence.

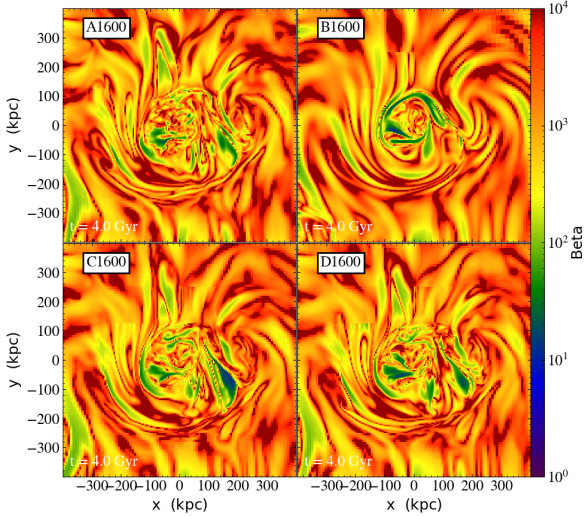


**Figure 7.** Slices of plasma  $\beta$  at  $t = 4.0$  Gyr for Cases A1600-D1600 simulations (initial  $\beta = 1600$ ). The overall plasma  $\beta$  values are high, indicating that even after shear amplification by the sloshing motions that magnetic fields are relatively weak and do not play a dominant role in the dynamics.

viscosity coefficient and a higher Reynolds number in the core region. Also, the gas velocities are higher within the cold front surfaces, also increasing the Reynolds number. Consequently, the inner regions are more prone to instability, making it easier for turbulence to develop through the growth of the KHI. In Figure 6, the dark blue regions just outside the cold front surfaces indicate that the effect of viscosity is stronger above the fronts, primarily due to the higher temperatures. In these regions,  $Re \lesssim 30$ , which according to Roediger et al. (2013a) should be low enough to suppress KHI. The smooth cold fronts in Case B1600 confirm this expectation. However, the cold fronts are not

nearly as smooth in the C1600 and D1600 cases, due to the fact that the effective Reynolds number has been increased due to the reduced viscosity from anisotropy and limits on the viscous flux imposed by microinstabilities.

The magnetic field can also play a crucial role in shaping the cold fronts. Magnetic tension suppresses the KHI of the cold front when the direction of the magnetic field aligns with the cold front surface and when the magnetic tension is strong enough (Landau & Lifshitz 1960; Chandrasekhar 1961). Additionally, the direction of the magnetic field can influence the suppression of KHI by viscosity, due to its anisotropic nature with respect to the local field line direction. In order to discern whether the KHI suppression is mainly caused by viscosity or magnetic tension, in Figure 7 we present slices of plasma  $\beta$  for Cases A1600-D1600. ZuHone et al. (2011) showed that the suppression of KHI by the magnetic field becomes significant when the plasma  $\beta$  value becomes less than  $\sim 10$ . Figure 7 shows that the plasma  $\beta$  near the cold front surfaces of all four cases ranges from  $\sim 100$  to 1000, suggesting that the suppression of the KHI in the high- $\beta$  cases is primarily due to viscosity rather than magnetic tension. Moreover, because of the initially high plasma  $\beta$  values, the magnetic field lines in Cases A1600-D1600 are largely passively evolved and stretched by the sloshing motions. As shown in Figures 4 and 5 in Section 3.1, the magnetic field exhibits layered structures well aligned with the cold front surfaces. This magnetic field configuration further aids the suppression of the KHI by anisotropic viscosity in Cases C1600 and D1600.

The simulation results are consistent with expectations. Case A1600, which lacks viscosity, exhibits the most unstable cold fronts. In contrast, Case B1600, which includes isotropic viscosity, produces the smoothest and most stable cold fronts. Both Case C1600 and Case D1600 employ anisotropic viscosity, but produce different outcomes. Case C1600 maintains relatively stable cold fronts, while Case D1600, in which the viscosity is limited by pressure-anisotropy bounds associated with microinstabilities, exhibits small ripple-like structures along the cold front surfaces similar to the inviscid case.

### 3.3 Simulations with $\beta = 100$

In this section, we present the low- $\beta$  cases to examine how the gas in the central region will evolve with a stronger initial magnetic field in addition to viscosity. Figures 8 and 9 show density and temperature slice plots, respectively, for the low- $\beta$  cases. As in Figure 2, the line integral convolution shows the velocity streamlines, indicating the shears at the cold front surfaces. Due to the stronger magnetic fields, Cases A100, B100, and D100 exhibit smoother cold front surfaces compared to the high- $\beta = 1600$  cases due to the suppression of the KHI by magnetic tension, in addition to the effect of viscosity where it is present. This is supported by Figures 10 and 11, which shows the plasma  $\beta$  and magnetic field strength slice plots at  $t = 4.0$  Gyr for the low- $\beta$  cases. For certain regions along the cold front surfaces, the  $\beta$  values drop to  $\sim 10$  or even lower because of the local enhancement of magnetic field strength due to stretching by the sloshing motions, consistent with the results of previous work by ZuHone et al. (2011). Unlike cases C1600 and D1600, cases C100 and D100 are very similar in appearance, due to the wider pressure anisotropy bounds (Eq. 9) when the plasma  $\beta$  is lower, which thus permit a larger viscous suppression than the  $\beta = 1600$  simulations. As in the  $\beta = 1600$  simulations, the inner cold fronts within  $r \sim 100$  kpc exhibit more indications of KHI (and thus more differences between the different cases with different viscosity models) than the outer cold front at  $r \sim 200$  kpc.

As we did for the  $\beta = 1600$  simulations, we plot the angle between

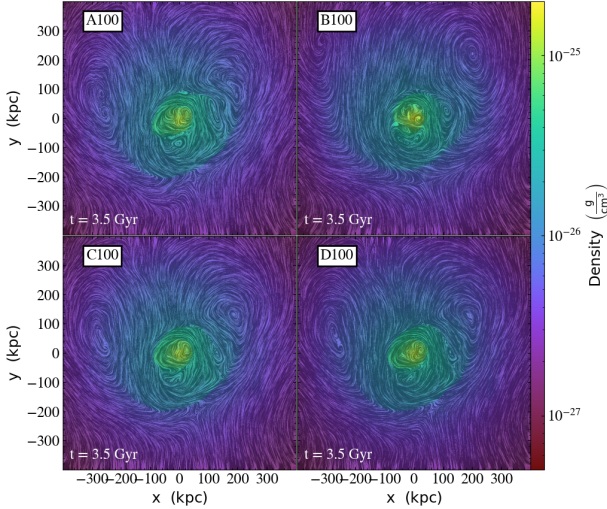


**Figure 8.** Density slice plots for the  $\beta \sim 100$  simulations at  $t = 4.0$  Gyr. With a stronger initial magnetic field, all four models exhibit more stable cold front surfaces compared to the weaker field cases. The black lines represent line integral convolution of the velocity field in the  $x$ – $y$  plane, used to visualise the gas velocity structure.

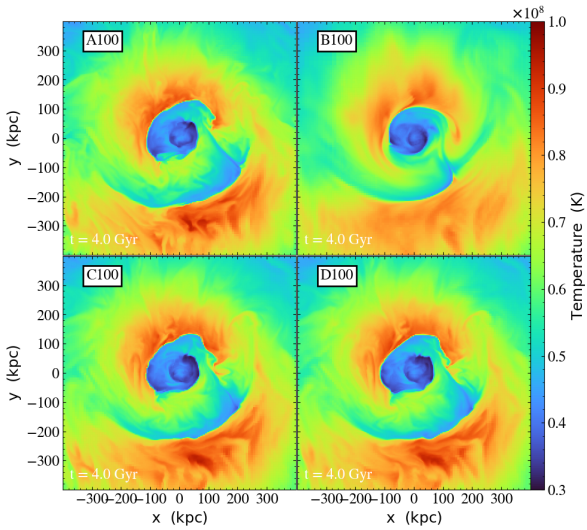


**Figure 9.** Temperature slice plots for the  $\beta \sim 100$  simulations at  $t = 4.0$  Gyr, highlighting the same features as Figure 8.

the magnetic field and the velocity vectors in Figure 12. As in Figure 5, the yellow regions indicate areas where  $|\cos \theta|$  is close to 1, signifying alignment between the magnetic field and the velocity directions produced by gas motions stretching the magnetic field. Compared to Figure 5, fewer regions have  $|\cos \theta| \approx 1$ , even near the cold front surfaces. In Cases A100, C100, and D100, these different degrees of alignment have a turbulent structure, as does the magnetic field strength itself. In Case B100, the isotropic viscosity damps turbulent motions such that the magnetic field structure is highly ordered, but there are nevertheless still clear divisions between

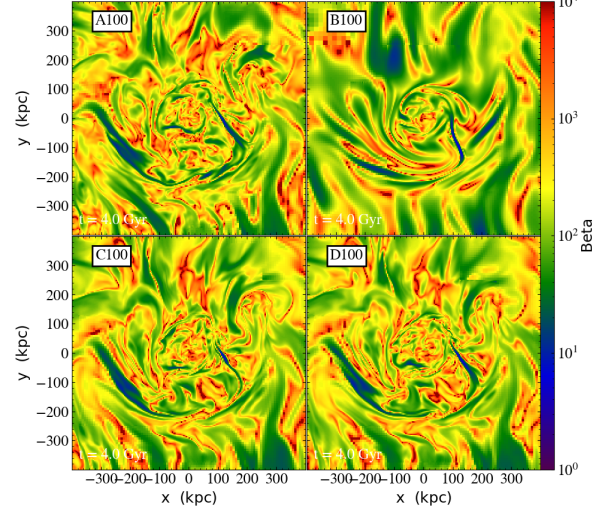


**Figure 10.** Slice plots for the plasma  $\beta$  at  $t = 4.0$  Gyr for the  $\beta \sim 100$  simulations. At some of the cold front surfaces,  $\beta \sim 10$  or even lower.

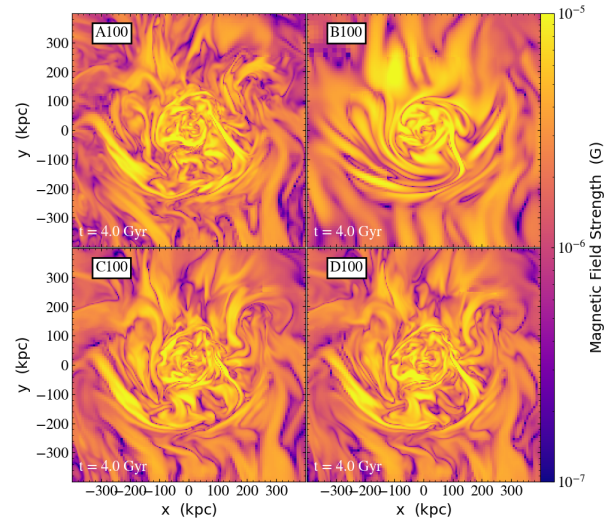


**Figure 11.** Magnetic field strength slice plots for low  $\beta$  ( $\beta \sim 100$ ) simulations at  $t = 4.0$  Gyr. Although the magnetic fields form layer-like structures similar to those in the  $\beta = 1600$  cases, its overall structure is more turbulent and disordered.

regions where the magnetic field and velocity vectors are parallel and those where they are not.

In the low- $\beta$  simulations, the magnetic tension is stronger, which results in the magnetic field lines becoming more resistant to becoming stretched by the velocity field. The most straightforward way to illustrate this is by the Alfvénic Mach number  $M_A = v/v_A$ , where  $v_A = B/\sqrt{4\pi\rho}$  is the Alfvén speed. Figure 13 shows the spatial distribution of  $M_A$  for all of the simulations with both values of  $\beta$ . The contrast between the two cases is substantial: the high- $\beta$  simulations exhibit large Alfvénic Mach numbers (with most regions having  $M_A > 5$ ), whereas the low- $\beta$  cases predominantly show  $M_A < 2$ . Large Alfvénic Mach numbers indicate that the plasma can

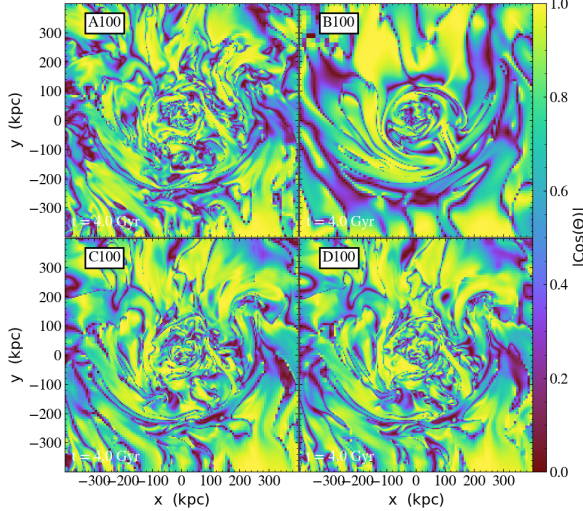


**Figure 12.** Angle between magnetic field and velocity slice plots for low  $\beta$  ( $\beta \sim 100$ ) simulations at  $t = 4.0$  Gyr. We use  $|\cos \theta|$  to present the figure, which ranges from 0 (not aligned) to 1 (aligned). There is a wider range of angles both inside and outside the cold fronts in these simulations than the  $\beta = 1600$  cases.

more easily drag or bend the magnetic field lines, indicating that the magnetic field amplification and the alignment effects discussed above are more readily triggered. In contrast, in the low- $\beta$  cases, with a lower  $M_A$ , the magnetic fields are less easily transported and stretched. Though the resulting misalignment with the cold front surfaces in the  $\beta = 100$  simulations would seem to lead to a lower suppression of KHI by the magnetic fields, the results are not that straightforward since most of the time there is some component of the field parallel to the front, and the overall field strength is higher than in the  $\beta = 1600$  cases.

#### 4 DISCUSSION

Our research follows the setup and discussion outlined by [ZuHone et al. \(2011, 2015\)](#). In [ZuHone et al. \(2011\)](#), the authors investigated how varying initial magnetic field strengths affect the sloshing motion in galaxy clusters. In a follow-up study, [ZuHone et al. \(2015\)](#) explored the impact of different viscosity models on the evolution and stability of cold fronts, though with only a weak initial magnetic field with  $\beta = 1000$ , and without considering the effect of microinstabilities. Here, we try to combine those two works and aim to delve deeper into the influence of magnetic field, and the case anisotropy viscosity limited by microinstabilities.

In the high- $\beta$  simulation ( $\beta \sim 1600$ ), our results are consistent with those of [ZuHone et al. \(2015\)](#). Case A fails to suppress the KHI, while Cases B (isotropic viscosity) and C (anisotropic viscosity) demonstrate varying degrees of KHI suppression. Our study shows that the pressure-anisotropy suppression effect of the microinstabilities (case D) further limits the ability of viscosity to suppress the KHI. Our results are also consistent with [ZuHone et al. \(2011\)](#), in that a stronger initial magnetic field provides stronger suppression of KHI. The stronger magnetic field also permits the pressure anisotropy to grow larger in case D100, which results in stronger viscous suppression compared with case D1600. However, in the cases with high plasma  $\beta$ , the magnetic field is more easily stretched by the sloshing motions

and aligned with the cold front surfaces, whereas in our low- $\beta$  cases the alignment effect is weaker. On the one hand, a magnetic field aligned with the front surface (as in our  $\beta = 1600$  simulations) provides maximal KHI suppression for a given field strength, but a partially aligned field with stronger field strength overall (the  $\beta = 100$  simulations) may nevertheless have a more noticeable effect. The effect on Braginskii viscosity from the varying magnetic field strength is twofold. The first is that a magnetic field more aligned with the front surface ( $\beta = 1600$  cases) will prevent viscous suppression until KHI produces an alignment between the local magnetic field and velocity gradient, whereas if the field is more tangled ( $\beta = 100$  cases) and is at least partially aligned with the velocity gradients to begin with, the suppression will be more immediate. Second, as already noted the stronger magnetic field permits stronger viscous flux. In complex situations such as modeled by our simulations, these effects can be difficult to disentangle from each other in a straightforward way.

There is another effect of the stronger initial magnetic field in the low- $\beta$  simulations that can complicate the interpretation of our results. Simulations of idealized cluster mergers such as the ones we use in this work are initialized with each cluster in hydrostatic equilibrium, with a high- $\beta$  turbulent magnetic field added in. As shown by [Chadayammuri et al. \(2022\)](#), such a tangled field produces seed velocity fluctuations when the magnetic tension inherent in the initial field relaxes. The resulting velocity perturbations can serve as the seed fluctuations for the KHI, potentially influencing the cold front morphology. This effect is more pronounced for lower initial  $\beta$ . The result is that the same simulations which are expected to be most effective at suppressing KHI growth via magnetic tension are also the ones which will have the strongest initial velocity perturbations to seed the KHI.

Finally, in theory Cases D100 and D1600 should more closely represent realistic ICM conditions, as they incorporate the regulation of Braginskii viscosity by kinetic microphysics. While these cases do develop indications of KHI at cold fronts, such structures are not necessarily inconsistent with observations, since some cold fronts have been found to exhibit evidence of KHI in deep X-ray exposures ([Wang & Markevitch 2018](#); [Werner et al. 2016](#); [Su et al. 2017](#)).

While this work was nearing completion, a similar study was being conducted by ZuHone et al. (in preparation), which investigates two relatively low- $\beta$  cases with Braginskii viscosity limited by microinstabilities. Our work was carried out independently and yields broadly consistent results, although some differences in the details remain due to variations in numerical resolution and initial conditions. In particular, the finest cell size in the other study is  $\Delta x = 0.98$  kpc, which is four times smaller than in our simulations. This higher resolution allows the development of finer-scale structures along the cold fronts, as the KHI has higher growth rates for small-scale perturbations. The implementation of the microinstability constraint in their study also differs slightly from ours, as they have considered a few variations of the hard-wall limiters motivated by recent plasma simulations. In addition, we include the isotropic viscosity cases to provide a direct comparison with the other models, though they do not. Due to their higher resolution, the inviscid cases in their simulations exhibit finer small-scale structures than the microinstability-limited cases. Nevertheless, our results and conclusions are broadly consistent, particularly in that the inclusion of pressure-anisotropy bounds makes the suppression of KHI by viscosity less effective, resulting in a morphology that more closely resembles the inviscid case. Also, in both works, for low- $\beta$  cases, higher magnetic field strengths play an important role in suppressing the KHI and widening the possible

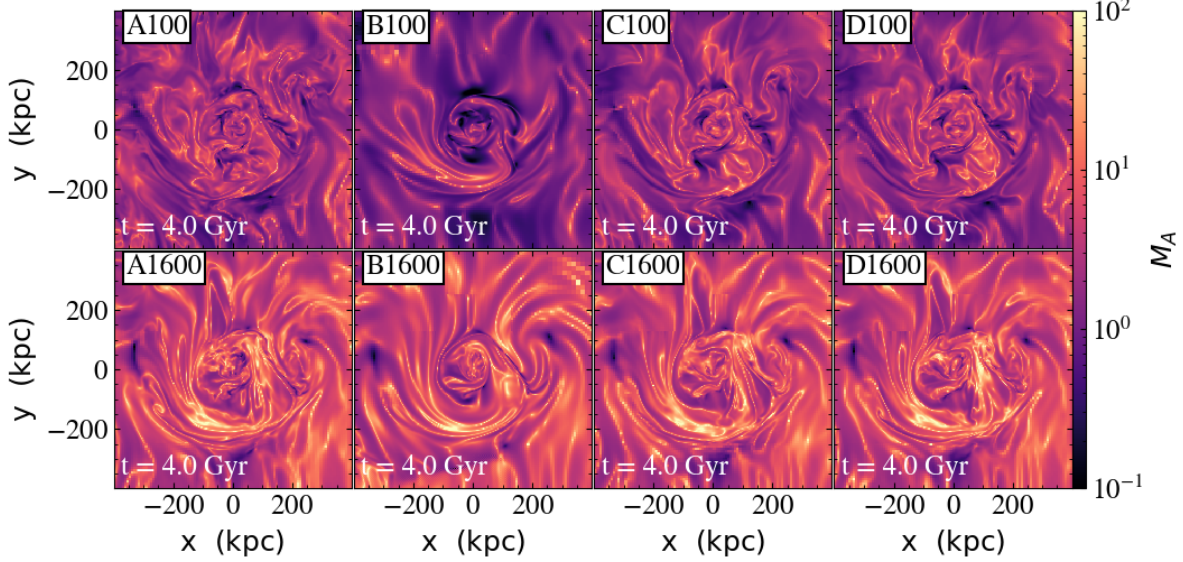


**Figure 13.** Alfvénic Mach number for all simulations at  $t = 4.0$  Gyr. The upper four slices correspond to the low- $\beta$  cases, while the lower four slices show the high- $\beta$  cases. The low- $\beta$  cases exhibit systematically lower Alfvén Mach numbers than the high- $\beta$  cases.

range of pressure anisotropy when the effects of microinstabilities are included.

## 5 CONCLUSIONS

In X-ray observations of the ICM, we find cold fronts in many merging clusters, which are believed to arise from sub-sonic motions of low entropy gas. Some observed cold fronts appear smooth, while others exhibit disruptions which resemble the effects of KHI. This may indicate that while some degree of viscosity is indeed present in the ICM, but the degree of KHI suppression varies from system to system. Such an observational diversity provides a valuable opportunity to constrain the microphysical properties of the ICM through comparison with numerical simulations. In our study, we utilized simulations with varying ICM viscosity models to assess the suppression of the KHI on the surfaces of cold fronts, with the aim of exploring the roles of ICM viscosity and magnetic tension. Specifically, we explore the effects of viscosity on sloshing cold fronts in galaxy clusters, utilizing Braginskii-MHD simulations. Our research follows the methodologies established by ZuHone et al. (2011), ZuHone et al. (2015), and Kingsland et al. (2019), with the goal of delving deeper into the influences of magnetic fields and anisotropic viscosity limited by microinstabilities. We performed a series of cluster merger simulations including four different viscosity models and two values of plasma  $\beta$ .

Our simulation results in the high plasma  $\beta$  cases ( $\beta \sim 1600$ ) are summarized as follows:

- Case A1600: Fails to suppress KHI, leading to disrupted cold fronts.
- Case B1600: Effectively suppresses KHI, resulting in smooth cold front surfaces.
- Case C1600: Demonstrates intermediate suppression of KHI, and the surfaces of cold fronts appear more stable.

- Case D1600: Does not effectively suppress KHI, similar to Case A, and forms small-scale perturbations at cold front surfaces.

These results suggest that, when the effect of magnetic tension is negligible, the smoothness of the cold fronts could in principle allow us to constrain the viscosity of the ICM. Several observational studies (Wang & Markevitch 2018; Werner et al. 2016; Su et al. 2017) have reported ripple-like structures along cold front surfaces and derived upper limits on the effective viscosity, suggesting that the full isotropic Spitzer viscosity (as in Case B) is too strong (which is already largely assumed on theoretical grounds alone). However, the differences between the other viscosity models are more subtle, and are at least qualitatively compatible with existing observations.

The simulation results for the low plasma  $\beta$  cases ( $\beta \sim 100$ ) are as follows:

- Case A100: Magnetic field suppresses the KHI, yielding smoother cold front surfaces compared to Case A1600.
- Case B100: Effectively suppresses the KHI, resulting in smooth cold front surfaces.
- Case C100: Shows slightly improved level of KHI suppression compared to A100.
- Case D100: The suppression of the KHI is more effective compared to D1600 and similar to Case C100, due to the wider pressure anisotropy bounds.

In the simulations with low plasma  $\beta$ , the strong magnetic field suppresses the perturbations and hence it is more difficult for the KHI to grow compared to the high- $\beta$  simulations. Therefore, in the low- $\beta$  cases, the cold front morphology for all viscous models is more similar (though Case B100 still has the most stable surface).

From the time when cold fronts were discovered shortly after the launch of *Chandra*, there have been attempts to place constraints on the ICM viscosity or the strength of the magnetic field layers at cold front surfaces from the presence or absence of KHI. Our simulations suggest that both of these effects can play an important

role in stabilizing cold fronts, but that their effects are difficult to disentangle from one another if the magnetic field is strong enough such that it both suppresses KHI by itself while also permitting a wider range of pressure anisotropies that will have the same effect.

## ACKNOWLEDGEMENTS

The simulations were performed using computational resources provided by the Center for Informatics and Computation in Astronomy (CICA) at National Tsing Hua University, funded by the Ministry of Education (MOE) of Taiwan. MHH and HYKY acknowledge support from National Science and Technology Council (NSTC) of Taiwan (NSTC 112-2628-M-007-003-MY3; NSTC 114-2112-M-007-032-MY3). HYKY acknowledges support from Yushan Scholar Program of the Ministry of Education (MoE) of Taiwan (MOE-108-YSFMS-0002-003-P1; MOE-114-YSFMS- 0002-002-P2). Support for JAZ was provided by the *Chandra* X-ray Observatory Center, which is operated by the Smithsonian Astrophysical Observatory for and on behalf of NASA under contract NAS8-03060. FLASH was developed in part by the DOE NASA- and DOE Office of Science-supported Flash Center for Computational Science at the University of Chicago and the University of Rochester. Data analysis presented in this paper was conducted with the publicly available *yt* visualization software (Turk et al. 2010).

## DATA AVAILABILITY

The data underlying this article will be shared upon reasonable request to the corresponding author.

## REFERENCES

Ascasibar Y., Markevitch M., 2006, *The Astrophysical Journal*, 650, 102–127  
 Barnes A., 1966, *Physics of Fluids*, 9, 1483  
 Bott A. F. A., Arzamasskiy L., Kunz M. W., Quataert E., Squire J., 2021, *ApJ*, 922, L35  
 Braginskii S. I., 1965, *Reviews of Plasma Physics*, 1, 205  
 Chadyammuri U., ZuHone J., Nulsen P., Nagai D., Russell H., 2022, *MNRAS*, 512, 2157  
 Chandrasekhar S., 1961, *Hydrodynamic and hydromagnetic stability*  
 Chandrasekhar S., Kaufman A. N., Watson K. M., 1958, *Proceedings of the Royal Society of London Series A*, 245, 435  
 Dubey A., Antypas K., Ganapathy M. K., Reid L. B., Riley K., Sheeler D., Siegel A., Weide K., 2009, *Parallel Computing*, 35, 512  
 Dursi L. J., 2007, *ApJ*, 670, 221  
 Fryxell B., et al., 2000, *ApJS*, 131, 273  
 Gary S. P., Wang J., Winske D., Fuselier S. A., 1997, *Journal of Geophysical Research: Space Physics*, 102, 27159  
 Hasegawa A., 1969, *Physics of Fluids*, 12, 2642  
 Hellinger P., 2007, *Physics of Plasmas*, 14, 082105  
 Hellinger P., Matsumoto H., 2000, *J. Geophys. Res.*, 105, 10519  
 Hellinger P., Trávníček P. M., 2008, *J. Geophys. Res.*, 113, A10109  
 Hernquist L., 1990, *ApJ*, 356, 359  
 Keshet U., Markevitch M., Birnboim Y., Loeb A., 2010, *ApJ*, 719, L74  
 Kingsland M., Yang H. Y. K., Reynolds C. S., Zuhone J. A., 2019, *ApJ*, 883, L23  
 Kunz M. W., Schekochihin A. A., Stone J. M., 2014, *Phys. Rev. Lett.*, 112, 205003  
 Landau L. D., Lifshitz E. M., 1960, *Electrodynamics of continuous media*  
 Ley F., Zweibel E. G., Miller D., Riquelme M., 2024, *The Astrophysical Journal*, 965, 155  
 Lyutikov M., 2006, *MNRAS*, 373, 73  
 Markevitch M., Vikhlinin A., 2007, *Phys. Rep.*, 443, 1  
 Markevitch M., et al., 2000, *ApJ*, 541, 542  
 Markevitch M., Gonzalez A. H., David L., Vikhlinin A., Murray S., Forman W., Jones C., Tucker W., 2002, *ApJ*, 567, L27  
 Melville S., Schekochihin A. A., Kunz M. W., 2016, *MNRAS*, 459, 2701  
 Parker E. N., 1958, *Physical Review*, 109, 1874  
 Roediger E., Kraft R. P., Nulsen P., Churazov E., Forman W., Brüggen M., Kokotanekova R., 2013a, *MNRAS*, 436, 1721  
 Roediger E., Kraft R. P., Forman W. R., Nulsen P. E. J., Churazov E., 2013b, *The Astrophysical Journal*, 764, 60  
 Rosenbluth M., 1956, Technical report, STABILITY OF THE PINCH, <https://www.osti.gov/biblio/4329910>. Los Alamos Scientific Lab., N. Mex., <https://www.osti.gov/biblio/4329910>  
 Schekochihin A., Cowley S., Kulsrud R., Hammett G., Sharma P., 2005, in Chyzy K. T., Otmianowska-Mazur K., Soida M., Dettmar R.-J., eds, *The Magnetized Plasma in Galaxy Evolution*. pp 86–92 (arXiv:astro-ph/0411781), doi:10.48550/arXiv.astro-ph/0411781  
 Southwood D. J., Kivelson M. G., 1993, *J. Geophys. Res.*, 98, 9181  
 Spitzer L., 1962, *Physics of Fully Ionized Gases*  
 Su Y., et al., 2017, *ApJ*, 834, 74  
 Tittley E. R., Henriksen M., 2005, *The Astrophysical Journal*, 618, 227  
 Turk M. J., Smith B. D., Oishi J. S., Skilling S. W., Abel T., Norman M. L., 2010, *The Astrophysical Journal Supplement Series*, 192, 9  
 Vikhlinin A., Markevitch M., Murray S. S., 2001, *ApJ*, 551, 160  
 Wang Q. H. S., Markevitch M., 2018, *ApJ*, 868, 45  
 Werner N., et al., 2016, *MNRAS*, 455, 846  
 ZuHone J. A., Markevitch M., Johnson R. E., 2010, *The Astrophysical Journal*, 717, 908  
 ZuHone J. A., Markevitch M., Lee D., 2011, *ApJ*, 743, 16  
 ZuHone J. A., Markevitch M., Ruszkowski M., Lee D., 2012, *The Astrophysical Journal*, 762, 69  
 ZuHone J. A., Kunz M. W., Markevitch M., Stone J. M., Biffi V., 2015, *ApJ*, 798, 90

This paper has been typeset from a *TeX/LaTeX* file prepared by the author.